Available online at BCREC website: https://bcrec.id

Bulletin of Chemical Reaction Engineering & Catalysis, 17 (2) 2022, 304-321

Research Article

Numerical Study of a Water Gas Shift Fixed Bed Reactor Operating at Low Pressures

Wail El-Bazi[1,*], Mustapha Bideq[2], Abderrahim El-Abidi[2], Said Yadir[2], Bajil Ouartassi[3]

[1]Laboratory of Process Engineering, Computer Science and Mathematics, Department of Process Engineering, National School of Applied Sciences, Sultan Moulay Slimane University, Bd Béni Amir, BP 77, 25000, Khouribga, Morocco.
[2]Laboratory of Materials, Processes, Environment and Quality (LMPEQ), National School of Applied Sciences, Cadi Ayyad University, Route Sidi Bouzid BP 63, 46000 Safi, Morocco.
[3]Laboratory of Process Engineering, Computer science and Mathematics, Department of Computer Science and Mathematics, National School of Applied Sciences, Sultan Moulay Slimane University, Bd Béni Amir, BP 77, 25000, Khouribga, Morocco.

Received: 26th January 2022; Revised: 26th February 2022; Accepted: 4th March 2022
Available online: 9th March 2022; Published regularly: June 2022

Abstract

Today, hydrogen has become one of the most promising clean energy. Several processes allow obtaining hydrogen, among them there is the Water Gas Shift (WGS) reaction. On an industrial scale, WGS reaction takes place at high pressure [25–35 bar]. At high pressure, the cost of the process rises due to the energy consumed by compression, and the reduction in the lifetime of the equipment and the catalyst. At low pressures, catalyst lifetime can reach many years and the energy cost is reduced. It is for this reason that we are interested in modelling and simulation of a WGS converter operating at low pressures close to atmospheric pressure. In this work, a numerical study was conducted in order to determine the conditions allowing good rector operating at low pressure. A number of drawbacks of the process were identified. These drawbacks are essentially the non-negligible pressure drops and the strong intraparticle diffusion resistances. The prediction of the concentrations and the reaction rate within the pellet showed that the active zone of the pellet is located near the particle surface. It has also been shown that the resistances to interfacial mass and heat transfer are insignificant. The study of pressure effect showed that the pressure increase reduces the required catalyst mass to achieve equilibrium. Finally, this work revealed that the decrease in temperature and the increase in the concentrations of the reactants by increasing their fluxes, make it possible to increase the effectiveness factor of the catalyst and the conversion of carbon monoxide.

Copyright © 2022 by Authors, Published by BCREC Group. This is an open access article under the CC BY-SA License (https://creativecommons.org/licenses/by-sa/4.0).

Keywords: Diffusion resistances; Effectiveness factor; Fixed bed; Orthogonal collocation; Thiele's modulus

How to Cite: W. El-Bazi, M. Bideq, A. El-Abidi, S. Yadir, B. Ouartassi (2022). Numerical Study of a Water Gas Shift Fixed Bed Reactor Operating at Low Pressures. *Bulletin of Chemical Reaction Engineering & Catalysis*, 17(2), 304-321 (doi: 10.9767/bcrec.17.2.13510.304-321)

Permalink/DOI: https://doi.org/10.9767/bcrec.17.2.13510.304-321

1. Introduction

Hydrogen is an ideal fuel due to its high-energy content and its compatibility with the environment. In order to generate this molecule from fossil fuels, biomass or synthesis gas (syngas), the WGS uses hydrogen from water steam and carbon monoxide [1]. This reaction is generally carried out in the presence of catalysts based on metals, such as Cu, Fe, Ni, Pd, Pt, Rh and Ru [2]. Metal oxides based on iron oxide or copper oxide are also used in the catalysis of this reaction [3].

In order to increase the conversion of carbon monoxide present in this balanced reaction,

* Corresponding Author.
Email: w.elbazi@usms.ma (W. El Bazi);
Telp: +212-61-4869374

manufacturers are implementing WGS in two fixed bed adiabatic catalytic reactors connected in series and comprising an intercooler [4]. In the first reactor, the reaction is carried out at high temperature (350–450 °C) in the presence of catalysts based on iron oxide and chromium(III) oxide (Cr_2O_3) [3]. In order to displace the equilibrium, the second reactor operates at lower temperatures (180–300 °C). Under these low temperature conditions, the catalysts used are based on copper or copper oxide with alumina oxide promoters (Al_2O_3). The promoters keep the catalyst from sintering [5]. This reaction is present in many industrial processes such as: DME synthesis [6], the Fischer-Tropsch Process [7], ammonia production [3], methanol synthesis [8] and Steam gasification processes [5]. Typically, WGS is carried out on an industrial scale at pressures between 25 and 35 bar [9].

Several researches have been interested in studying the chemical kinetics of this reaction. The mathematical expressions obtained corresponding to HT or LT catalysts often take the form of a power law model comprising a factor β taking into account the reverse reaction [10–15]. This power law is widely used in modelling and simulation studies, which are effective tools in the design, diagnosis and optimization of WGS reactors operation. The literature is rich in a large number of works interested in the numerical study of these converters using several phenomenological models.

The least mathematically complicated models are the mono-dimensional pseudo-homogeneous steady state models. These models do not take into account the limitations of inter and intraparticle transfer phenomena, that is why they are rather suitable for low volume reactors with small diameter catalytic pellets (<0.5 mm) [15]. Maklavany *et al*. [16] developed a pseudo-homogeneous model with axial dispersion to study the behavior of a small isothermal reactor operating at low pressures (1.2 - 1.65 bar) and at low temperatures. In this study, a multi-objective optimization led to the determination of the optimal operating conditions giving a significant increase in hydrogen productivity [16].

It should be noted that the fixed bed reactors found in industry have large volumes and large diameter catalytic pellets [15]. Under these conditions, the resistances to inter and intraparticle transfer of mass and heat should be taken into account. To diagnose, size and predict the behavior of these converters, the mono-dimensional heterogeneous model offers great precision for the design of reactors operating in steady state [17]. Many authors have adopted this model for the study of WGS reactors operating at medium and high pressures [4,18–20]. These works have shown that generally, the catalytic pellet can be considered isothermal, but the limitations to the intraparticle transfer of mass cannot be neglected [4]. It was also shown that choosing an optimal temperature profile allows significant improvements in the conversion of carbon monoxide [18]. This model can correctly describe the behaviour of industrial reactors despite the presence of H_2S in the reaction mixture [19]. The use of the optimization rate Ro in thermal management and in the design of the reactor allows considerably reducing the catalytic masses [20]. Another study was interested in reactors operating at low pressures [1-4 atm] and temperatures compared this model to 2D-model. In this paper, it has been found that radial gradients of mass and heat can be neglected and that the 1D heterogeneous model is sufficient for steady-state considerations [21].

When steady state is not achieved, the use of a dynamic model to describe the behavior of the reactor is necessary. Other conditions require the use of more than one-dimensional models, such as: the non-adiabaticity of the reactor, the extreme exothermicity of the reaction [18,22], or even, when the reaction is produced in a membrane reactor [23]. To study these cases, other works adopting more complex heterogeneous models were carried out [15,23-25]. These studies highlighted the risk associated with the possible overheating of catalysts when starting up the industrial unit before reaching steady state [15], they show that the location of a cooler inside the catalytic bed affects carbon monoxide conversion [24], and that one-dimensional models are not suitable for the membrane reactor [23]. Thanks to the 3D model developed, it was also possible to predict the partial pressure distribution of hydrogen and carbon monoxide in the longitudinal and radial direction of a cylindrical part of the reactor [25].

Other numerical studies were conducted independently of the reactor as the Levent's theoretical study, which was carried out on a spherical iron oxide-chromia catalyst pellet under high pressure and temperature conditions. This study revealed that the intraparticle temperature gradients are much smaller than the interfacial temperature gradients. At the same time, it has been shown that the mass transfer limitations within the pellet should not be neglected when the temperature exceeds 600 K [26].

Copyright © 2022, ISSN 1978-2993

Those simulation and modelling studies allowed a better prediction of the reactors behaviour and important optimization in their design. However, there are not many papers in literature that have focused on studying the behavior of large-scale WGS reactors operating at pressures approaching atmospheric pressure. In fact, operating at this pressure conditions can be useful, for instance in the steam gasification process to recover the syngas leaving the gasification reactor at low pressure [5]. In addition, operating at low pressures reduces energy consumption due to the compression and increases considerably the lifetime of the catalyst [27,28]. At the same time, under these conditions, the pressure drops compared to the inlet pressure are not negligible [5,28], the catalytic activity is disadvantaged [4,5,29] and the intraparticular diffusion is governed by the Knudsen regime [30,31]. Therefore, an in-depth numerical study of the behavior of reactors operating at low pressure allowing the prediction of the evolution of the various parameters in the Bulk phase and inside the catalytic pellet is of great importance. This kind of study makes it possible to define the operating conditions and the characteristics of the catalyst and the reactor necessary for the implementation of large-scale WGS converters operating at pressures slightly above atmospheric pressure. This work carried out does adequately meet these purposes.

To achieve these objectives, several one-dimensional models have been developed (rigorous heterogeneous model, heterogeneous model adopting the Thiele's approach, and pseudo-homogeneous model). To validate the rigorous model that we have developed, we compared the results obtained with the experimental and numerical results that exist in the literature.

The pseudo-homogeneous model was used to predict the behavior of the installation without the limitations to transfer phenomena and Thiele's approach was exploited in order to evaluate the possibility of predicting the behavior of the reactor in the simplest way.

In this study, we are interested in the evaluation of mass and heat transfer resistances and their impact on the behavior of the converter. In order to determine the active zone in the pellet when the pressure level is low, the intraparticle concentration and reaction rate profiles were predicted for different axial positions in the reactor.

Finally, in order to study the effects of some operating parameters on the yield of the process, we have been interested in the effects of the pressure, the temperature and the flow rate of reactants on the effectiveness factor of the catalyst and on various parameters at the outlet of the reactor.

2. Chemical Kinetics and Characteristics of the Catalyst

The WGS reaction is expressed by the equation:

$$CO + H_2O \rightleftharpoons CO_2 + H_2 \quad \Delta H_{R(298K)} = -41.2\,\text{kJ.mol}^{-1} \quad (1)$$

The expression of intrinsic chemical kinetics adopted here is proposed by Keiski *et al.* [12]:

$$-r_{CO} = 3714.5 \exp\left(\frac{-66578.512}{R_g T}\right) C_{CO}^{0.54} C_{H_2O}^{0.1} (1-\beta) \quad (2)$$

With:

$$\beta = \frac{C_{CO_2} C_{H_2}}{C_{CO} C_{H_2O}} \frac{1}{K_e} \quad (3)$$

$$K_e = \exp\left(\frac{4577.8}{T} - 4.33\right) \quad (4)$$

where $-r_{CO}$ is the rate of the WGS reaction (mol.kg^{-1}.s^{-1}), R_g is the universal gas constant (8.3144 J.K^{-1}.mol^{-1}), C_i is the concentration of species i (mol.m^{-3}), and K_e is the equilibrium constant of the WGS reaction. The catalyst used is based on Fe_3O_4-Cr_2O_3, the properties of this catalyst are given in Table 1 [12].

3. Process and Modeling

3.1 Process Description

The catalytic reactor considered is an adiabatic multi-tubular fixed bed reactor. These tubes are packed with the catalyst and fed with a reaction mixture with a flow of 2670.61 kg.h^{-1}. This flux was chosen to study a feed flux of real order of magnitude, because it corresponds to one of the total fluxes feeding the pilot reactors as reported by van Dijk *et al.* [19] and Rosner *et al.* [20].

Table 1. Catalyst characteristics.

Particle diameter (d_P, m)	Shape	Density of solid (ρ_s, kg.m^{-3})	Thermal conductivity of solid (λ_S, W.m^{-1}.K^{-1})	Intragranular porosity (ε_C)	Average pore size (d_{pore}, m)	Pore tortuosity (τ)
2×10^{-3}	Spherical	1945	0.3	0.48	9×10^{-9}	4

Copyright © 2022, ISSN 1978-2993

The characteristics of the reactor and the specifications of the feed streams are presented in Table 2. To study the effect of temperature on the behaviour of the reactor, other simulations were carried out for other feed temperatures, while keeping the other operating conditions and the same characteristics of the reactor (Table 2).

The composition chosen corresponds well to that studied to establish the kinetic expression that we used in this paper and which is presented in Equation (2) [12], the H_2O/CO ratio and the temperatures chosen also enter into the range of H_2O/CO ratios and temperatures tested for the establishment of this kinetic expression [12]. In addition, this composition is in perfect agreement with that of the gas stream at the outlet of a gas reforming reactor derived from coal or biomass characterized by significant hydrogen fractions [23]. The choice of the high H_2O/CO ratio is motivated also by practical reasons. Indeed, when the H_2O/CO ratio is low, there is formation and deposition of carbon on the pellets leading to a deactivation of the catalyst, which is not taken into account in the models developed [32].

In order to evaluate the effect of the pressure on the behavior of the reactor, other simulations were carried out for different values of the feed pressure (P_0 = 9.87 atm, P_0 = 4.93 atm), while keeping the other operating conditions and the same characteristics of the reactor (Table 2).

The study of the effect of the reactants flow rates on the process required the realization of other simulations for other reactants feedstreams, while the other operating conditions, the H_2O/CO ratio (H_2O/CO = 5) and the characteristics of the reactor have not been changed (Table 2).

Table 2. Characteristics of the reactor and the feed stream taken into account in the simulation.

Fixed bed reactor	
Number of tubes (N_t)	317
Diameter of tube (D_t, m)	0.09
Length of tube (L_t, m)	1
Feed stream of species i ($F_{i,0}$, mol.s^{-1})	
$F_{N2,0}$	7.097
$F_{H2,0}$	19.337
$F_{H2O,0}$	12.095
$F_{CO2,0}$	4.977
$F_{CO,0}$	2.419
Feed stream operating conditions	
Feed temperature (T_0, K)	650
Feed pressure (P_0, Pa)	121560

In order to validate the rigorous model developed, we carried out other simulations taking into account the operating conditions, the characteristics of the reactors and the size of the catalyst pellets as reported by Marin *et al.* [23] and Sanz *et al.* [32].

3.2 Modelling

The calculation code used to solve this problem has been developed under Matlab software.

3.2.1 Assumptions and justifications

We have considered that the catalyst pellets are isothermal, because it was verified that [26,33]:

$$\Delta T_{\max} = \left|\frac{\Delta H_R.D_{e,CO}.C_{COs}}{\lambda_e}\right| < \left|\frac{\Delta H_R.D_{e,CO}.C_{COf}}{\lambda_e}\right| < 0.02K \quad (5)$$

where, ΔT_{max} is the maximum temperature variation between the center and the surface of the pellet (K), ΔH_R is the enthalpy of the WGS reaction (J.mol^{-1}), $D_{e,CO}$ is the effective diffusion coefficient of CO (m^2.s^{-1}), C_{COs} is CO concentration at the surface particle (mol.m^{-3}), C_{COf} is CO concentration in the bulk phase (mol.m^{-3}), and λ_e is the effective thermal conductivity (J.m^{-1}.s^{-1}.K^{-1})

We can calculate the axial dispersion coefficient of CO ($D_{CO,ax}$, m^2.s^{-1}) by using equation [34]:

$$D_{CO,ax} = \left(\frac{\varepsilon_b\sqrt{\varepsilon_b}}{\mathrm{Re}.Sc_{CO}} + 0.5\right)u_s d_p \quad (6)$$

where, ε_b is the porosity of the catalytic bed, Re is the Reynolds number, Sc_{CO} is the Schmidt number of CO, and u_s is the superficial velocity (m.s^{-1}).

It has been found that Re>10, ($L_t/D_{CO,ax}$)>300 and the reactor is known to be adiabatic. Under these conditions, we can neglect the two modes of dispersion (axial and radial) [33]. Therefore, the use of one-dimensional models without dispersions and neglecting intraparticle temperature gradients is acceptable.

3.2.2 Catalyst pellet model

a. Rigorous model

The tortuous pores contained in the catalyst pellets are sites of diffusive mass transfer and chemical reaction. The intraparticle mass balance equations are written [6]:

Copyright © 2022, ISSN 1978-2993

For the reactants:

$$D_{e,i}\frac{1}{r^2}\frac{d}{dr}\left(r^2\frac{dC_i}{dr}\right)+\rho_s F_{pres} r_{CO}=0 \quad (7)$$

where, $D_{e,i}$ is the effective diffusion coefficient of species i ($m^2.s^{-1}$), r is the particle radial coordinate (m), and F_{pres} is the pressure scale-up factor.

For the products:

$$D_{e,i}\frac{1}{r^2}\frac{d}{dr}\left(r^2\frac{dC_i}{dr}\right)-\rho_s F_{pres} r_{CO}=0 \quad (8)$$

In the center of the particle, the concentrations of the reactants are minimal whereas the concentrations of the products are maximal. We can then express the boundary conditions equations corresponding to this intraparticle position ($r = 0$) as follows:

$$\frac{dC_i}{dr}(r=0)=0 \quad (9)$$

The pellet is surrounded by a film where convective transfers of mass and heat take place. One can then establish the equations of the boundary conditions corresponding to the surface of the particle ($r = R$) as follows:

$$K_{C,i}\left(C_{i,f}-C_{i,s}\right)=D_{e,i}\frac{dC_i}{dr}(r=R) \quad (10)$$

$$hA_p\left(T_s-T_f\right)=\bar{r}\rho_s F_{pres}\Delta H_r V_p = \eta_s r_{COs}\rho_s F_{pres}\Delta H_r V_p \quad (11)$$

where, $K_{C,i}$ is the mass-transfer coefficient of species i ($m.s^{-1}$), $C_{i,f}$ is the species i concentration in the bulk phase ($mol.m^{-3}$), $C_{i,s}$ is the species i concentration at the surface particle ($mol.m^{-3}$), h is the heat-transfer coefficient ($J.s^{-1}.m^{-2}.K^{-1}$), A_p is the particle surface (m^2), T_s is the temperature of the surface of the pellet (K), T_f is the temperature of the bulk gas (K), $\bar{r}$ is the apparent reaction rate ($mol.kg^{-1}.s^{-1}$), V_p is the particle volume (m^3), η_s is the Particle effectiveness factor, and r_{COs} is the reaction rate under surface conditions ($mol.kg^{-1}.s^{-1}$).

At steady state, the rate of reactant consumption within the particle is equal to the rate of mass fluxes transferred from the Bulk to the particle exterior surface [30]. We can then arrive at the following equation valid for the reactants:

$$h\left(T_s-T_f\right)=-D_{e,i}\frac{dC_i}{dr}(r=R)\Delta H_r \quad (12)$$

where, R is the particle radius (m).

For the products, we use the following equation:

$$h\left(T_s-T_f\right)=D_{e,i}\frac{dC_i}{dr}(r=R)\Delta H_r \quad (13)$$

The intraparticle and the surface of the catalyst concentrations of the various chemical species involved in the reaction, as well as the surface temperature are obtained by solving the system of Equations (7)–(10) and Equation (12) applied to carbon monoxide. To perform this resolution, we adopted the orthogonal collocation method, which is the most suitable technique for this kind of differential equations (diffusion-reaction) [35]. Resolutions are done using different numbers of internal collocation points. The concentrations obtained corresponding to the points of collocation (internal, in the center of the pellet and at the surface of the pellet) are exploited to estimate the reaction rates within and at the surface of the particle, which makes it possible to calculate the overall effectiveness factor (η_e) using the equation [30]:

$$\eta_e=\frac{1}{r_{COf}.V_p}\int_0^R r_{CO}(r).4\pi r^2 dr \quad (14)$$

where, r_{COf} is the reaction rate under Bulk conditions ($mol.kg^{-1}.s^{-1}$), which is calculated using the Bulk phase concentrations and temperature:

$$-r_{COf}=F_{pres}3714.5\exp\left(\frac{-66578.512}{R_g T_f}\right)C_{COf}^{0.54}C_{H_2Of}^{0.1}\left(1-\frac{C_{CO_2f}C_{H_2f}}{C_{COf}C_{H_2Of}}\frac{1}{K_e}\right) \quad (15)$$

b. Generalized Thiele's model

This approach is adopted by some authors to study the behavior of fixed bed catalytic reactors. For example, the WGS reactors [24], or even the converters of dehydrogenation of 1-Butene into Butadiene [36]. This model can be relatively misleading in the case of the intermediate regime [37], but remains relatively less complicated mathematically than the rigorous model.

Thiele's modulus (Φ_s) is expressed by the following equation [37]:

$$\Phi_s=\frac{\frac{dp}{6}\left(-r_{COs}\right)}{\left(2D_{e,CO}\int_{C_{CO,eq}}^{C_{CO,s}}-r_{CO}dC_{CO}\right)^{0.5}} \quad (16)$$

The particle effectiveness factor is calculated using the mathematical expression:

$$\eta_s=\frac{1}{\Phi_s}\left(\frac{1}{\tanh\left(3\Phi_s\right)}-\frac{1}{3\Phi_s}\right) \quad (17)$$

It is possible to make some simplifications to express C_{H2O}, C_{CO2} and C_{H2} according to C_{CO} [36].

Copyright © 2022, ISSN 1978-2993

- for H_2O:

$$C_{H_2O} = C_{H_2O,s} + \frac{D_{e,CO}}{D_{e,H_2O}}\left(C_{CO} - C_{CO,s}\right) \quad (18)$$

- for the products:

$$C_i = C_{i,s} + \frac{D_{e,CO}}{D_{e,i}}\left(C_{CO,s} - C_{CO}\right) \quad (19)$$

Dividing Equation 12 or 13 over Equation 10 expresses $C_{i,s}$ in terms of $C_{i,f}$, T_s, and T_f.

- for the reactants, we have the following expression:

$$C_{i,s} = C_{i,f} + \frac{h}{K_{C,i}\Delta H_r}\left(T_s - T_f\right) \quad (20)$$

- for the products, we use the equation:

$$C_{i,s} = C_{i,f} - \frac{h}{K_{C,i}\Delta H_r}\left(T_s - T_f\right) \quad (21)$$

To calculate the overall effectiveness factor from the particle one, we use the expression:

$$\eta_e = \frac{\eta_s r_{CO,s}}{r_{CO,f}} = \frac{\bar{r}}{r_{CO,f}} \quad (22)$$

Equations (11) and (16)–(22) are used in an iterative calculation in order to be able to calculate η_e. The calculation of $C_{CO,eq}$ is done by solving the equation $r_{CO} = 0$ using the Newton-Raphson's method.

3.2.3 Fixed-bed reactor model

a. One-dimensional heterogeneous model [38]:

The equations of the model are derived from the continuity equation for the key component, CO, and the steady-state system energy balance, as follows:

Mass balance:

$$\frac{dX_{CO}}{dZ} = \frac{-\eta_e r_{CO} F_{pres} \rho_B S}{F_{CO,0}} \quad (23)$$

where, X_{CO} is the carbon monoxide conversion, Z is the reactor axial coordinate (m), ρ_B is the apparent density of the bed (kg.m^{-3}), and S is the reactor tube cross section (m^2).

Energy balance for an adiabatic reactor:

$$\sum F_i C_{pi} \frac{dT}{dZ} = \eta_e \Delta H_R r_{CO} F_{pres} \rho_B S \quad (24)$$

where, C_{pi} is the heat capacity at constant pressure of species i (J.mol^{-1}.K^{-1}), and T is the temperature (K).

The validation of the rigorous model required the establishment of an energy balance for an isoperibolic reactor:

$$\sum F_i C_{pi} \frac{dT}{dZ} = \eta_e \Delta H_R r_{CO} F_{pres} \rho_B S - h_w \pi D_t \left(T - T_w\right) \quad (25)$$

where, h_w is the wall heat transfer coefficient (W.m^{-2}.K^{-1}), and T_w is the wall temperature (K).

The pressure drop along the bed is evaluated by using Ergun's equation:

$$\frac{dP}{dZ} = -f\frac{\rho u_s^2}{d_p} \quad (26)$$

where, P is the pressure (Pa), f is the friction factor, and ρ is the density of fluid (kg.m^{-3}).

To perform the numerical resolution, we first divide the axial length of the reactor tube into 200 sections. At the inlet of each section, the effectiveness factor is calculated (paragraph 3.2.2). Subsequently, this factor is introduced into the ordinary differential Equations (23) and (24) for an adiabatic reactor, or into the ordinary differential Equations (23) and (25) for an isoperibolic reactor. The ODE system (Equations (23), (24), and (26)) for an adiabatic reactor, or the ODE system (Equations (23), (25), and (26)) for an isoperibolic reactor was solved by the RK4 method. Through this procedure, the effectiveness factor corresponding to each section is determined and therefore the effectiveness factor profile along the installation, as well as the carbon monoxide conversion profile, temperature profile and pressure profile. The validation of the rigorous model required also the study of an isothermal reactor. In this case, the Equations (24) and (25) were not used.

b. Mono-dimensional pseudo-homogeneous model [38]:

The System of ordinary differential equations related to this model is the same as that presented in the previous paragraph, but with $\eta_e = 1$. Therefore, the numerical method used is the same, but without the need to calculate the effectiveness factor.

3.2.4 Complementary equations

Table 3 shows the formulas and equations used for the estimation of the other parameters corresponding to the models studied.

4. Results and Discussion

4.1 Estimation of the Effectiveness Factor and Determination of Resistance Limiting Transfer Phenomena

Figure 1 shows the profiles of the overall effectiveness factor η_e, along the reactor using the rigorous model and adopting different numbers of internal collocation points. We notice that the 3 profiles are close and that the ef-

Copyright © 2022, ISSN 1978-2993

Table 3. Correlations and auxiliary equations.

Diffusion coefficients

$$D_{e,i} = 4850 d_{pore} \left(\frac{T}{M_i} \right)^{0.5} \frac{\varepsilon_C}{\tau} \times 10^{-4} \quad (27) \qquad \text{if } 1 > d_{pore} \text{ with: } \quad l = \frac{R_g T}{P N_A \sigma^2 \pi \sqrt{2}} \quad (28) \qquad [30,31]$$

where, M_i is the molecular weight of species i (kg.mol^{-1}), l is the mean free path (m), N_A is the Avogadro constant (6.02214076×10^{23} mol^{-1}), and σ is the average diameter of molecules (m).

$$D_{i,m} = \left(1 - y_i\right) \left(\sum_{j=1, i \neq j}^{N} \frac{y_i}{D_{i,j}} \right)^{-1} \quad (29) \qquad [18]$$

where, $D_{i,m}$ is the molecular diffusion coefficient in the gas mixture (m^2.s^{-1}), $D_{i,j}$ is the binary diffusion coefficient (m^2.s^{-1}), and y_i is the mole fraction of component i. The formulas related to the calculation of $D_{i,j}$ are available in [18].

Thermal conductivities

$$\lambda_e = \lambda_g \left(\varepsilon_C + \frac{1 - \varepsilon_C}{0.139 \varepsilon_C - 0.0339 + 6.667 \lambda_g} + 0.75 \varepsilon_C \, \mathrm{Pr} \, \mathrm{Re} \right) \quad (30) \qquad [39]$$

where, λ_g is the gas-mixture thermal conductivity (J.m^{-1}.s^{-1}.K^{-1}), and Pr is the Prandtl number.

with:
$$\lambda_g = \frac{\sum_i \lambda_i y_i \sqrt[3]{M_i}}{\sum_i y_i \sqrt[3]{M_i}} \quad (31) \qquad [16]$$

where, λ_i is the thermal conductivity of species i (J.m^{-1}.s^{-1}.K^{-1}). The expressions of λ_i according to the temperature are detailed in [15].

Viscosities

$$\mu = \sum_{i=1}^{N} \frac{y_i \mu_i}{\sum_{j=1}^{N} y_j \sqrt{\frac{M_j}{M_i}}} \quad (32) \qquad [16]$$

where, μ is the dynamic gas-mixture viscosity (kg.m^{-1}.s^{-1}), and μ_i is the dynamic viscosity of species i (kg.m^{-1}.s^{-1}). The expressions of μ_i according to the temperature are given in [15].

Heat capacities

$$C_p = \frac{\sum y_i C_{pi}}{M_m} \quad (33) \qquad \text{with:} \quad M_m = \sum y_i M_i \quad (34) \qquad [33]$$

where, C_p is the specific heat capacity of the gas mixture (J.kg^{-1}.K^{-1}), and M_m is the molecular weight of the gas mixture (kg.mol^{-1}). The expressions of C_{pi} according to the temperature are detailed [15].

Flow rates and velocities

$$F_{reactant} = F_{i,0} - F_{CO,0} X_{CO} \quad (35), \qquad F_{product} = F_{i,0} + F_{CO,0} X_{CO} \quad (36) \qquad [28]$$

$$G = \sum_{i=1}^{n} \frac{F_i M_i}{S} \quad (37), \qquad u_s = \frac{G}{\rho} \quad (38) \qquad \text{with:} \quad \rho = \frac{P}{R_g T} \sum_{i=1}^{i=n} y_i M_i \quad (39) \qquad [33]$$

where, G is the superficial mass velocity (kg.m^{-2}.s^{-1}).

Dimensionless numbers

$$\mathrm{Re} = \frac{G.d_p}{\mu} \quad (40), \qquad \mathrm{Pr} = \frac{\mu C_p}{\lambda_g} \quad (41) \qquad Sc_i = \frac{\mu}{\rho D_{i,m}} \quad (42) \qquad [33]$$

Copyright © 2022, ISSN 1978-2993

Table 3. …. (continued)….

Bed porosity	
$\varepsilon_B = 0.38 + 0.07\left[1 - \frac{\left[\frac{D_t}{d_p} - 2\right]^2}{\left(\frac{D_t}{d_p}\right)^2}\right]$ (43)	[19]
Mass and heat transfer coefficients	
$K_{C_i} = u_s Sc_i^{-2/3}\,\mathrm{Re}^{-0.41}.\frac{0.454}{\varepsilon_B}$ (44)	[33]
$h = 1.2K_{C_i} Sc_i^{2/3}\,\mathrm{Pr}^{-2/3}\,\rho C_p$ (45)	[30]
Molar concentration of species i	
$C_i = \frac{y_i P}{R_g T}$ (46)	[28]
Pressure scale-up factor	
$F_{pres} = P(atm)^{\left(0.5 - \frac{P(atm)}{250}\right)}$ (47)	[15]
Bed density	
$\rho_B = \left(1 - \varepsilon_B\right)\rho_s$ (48)	[38]
Heat of reaction	
$\Delta H_R = -4.12\times10^4 + \int_{298}^{T}\left(C_{p,CO_2} + C_{p,H_2} - C_{p,CO} - C_{p,H_2O}\right)dT$ (49)	[15]
Friction factor	
$f = \frac{1-\varepsilon_B}{\varepsilon_B^3}\left(a + b\frac{1-\varepsilon_B}{\mathrm{Re}}\right)$ with: a = 1.75 and b = 150 (50)	[38]
Catalytic mass Corresponding to a longitudinal position Z	
$w(Z) = S.Z.\rho_B$ (51)	[28]
where, w is the mass of catalyst (kg).	
Resistances to external heat and mass transfer	
$f_e = \frac{C_{COf} - C_{COs}}{C_{COf}}$ (52), $\alpha_e = \frac{T_s - T_f}{T_f}$ (53)	[30]
where, f_e is the fraction of resistance to external mass transfer, and α_e is the fraction of resistance to external heat transfer.	

Copyright © 2022, ISSN 1978-2993

fectiveness factor profiles corresponding to 7 and 8 points are almost identical. In the rest of this work, we adopt the results corresponding to 8 internal collocation points.

From this figure, there is a decrease in the effectiveness factor along the installation until the equilibrium is reached (Z ≈ 0.245 m), where this factor stabilizes at a value of 0.156. This drop in η_e, which signifies an increase in resistances to transfer phenomena, may be due to several reasons, such as: the increase of temperature or even the evolution of the concentrations of the different chemical species involved in the reaction along the reactor. We are going to explain this decrease in the effectiveness factor in more detail later in this paper.

In order to determine the resistances to the transfer phenomena responsible for these low values of η_e, we first evaluated the resistances to the mass transfer and interparticle heat. To do this, we estimated the profile of f_e and α_e along the reactor (Figures 2 and 3).

Figure 2 shows that f_e at the inlet of the reactor has a low value which is less than 6×10^{-3} and decreases further when moving forward in the reactor to the longitudinal position of 0.3, where f_e becomes zero and keeps this value through the installation. α_e also follows the same trend, but with an even lower value at the reactor inlet ($\alpha_e \approx 3.35\times10^{-4}$) and canceling out at the same longitudinal position as before. The decrease in f_e and α_e, and therefore, the decrease in the concentration and interparticle temperature gradients, is the consequence of approaching the equilibrium (chemical and thermodynamic) by advancing in the reactor. These very low values of f_e and α_e indicate that the resistances to interparticle transfer of mass and heat are negligible. In addition, the grain has been shown to be isothermal, which results in the absence of heat transfer resistances within the pellet. Therefore, the system is dominated by intraparticle diffusional resistances.

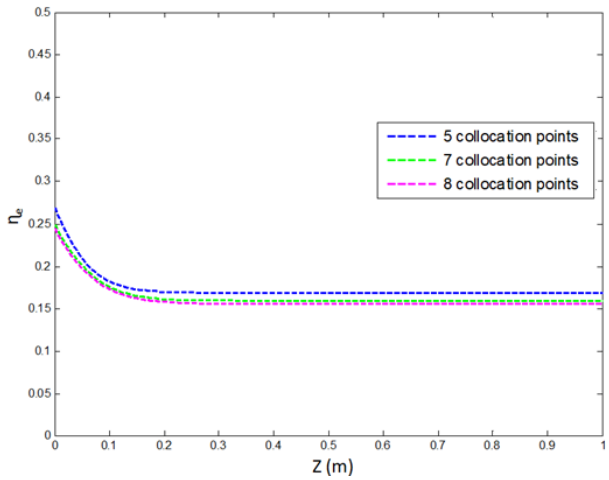


Figure 1. Overall effectiveness factor (η_e) *vs.* reactor length (Z(m)).

4.2 Validation of the Proposed Model

In order to validate the rigorous heterogeneous model developed, we proceeded to the comparison of the results obtained with the experimental and numerical results we found in the literature, under similar operating conditions. The first comparison was made with the experimental study conducted by Sanz *et al.* [32], which is carried out on a laboratory fixed-bed isothermal reactor. We took into consideration all the operating conditions and the characteristics of the catalyst and the reactor, which are detailed in reference [32]. For the catalytic particle model, we used our spherical grain model,

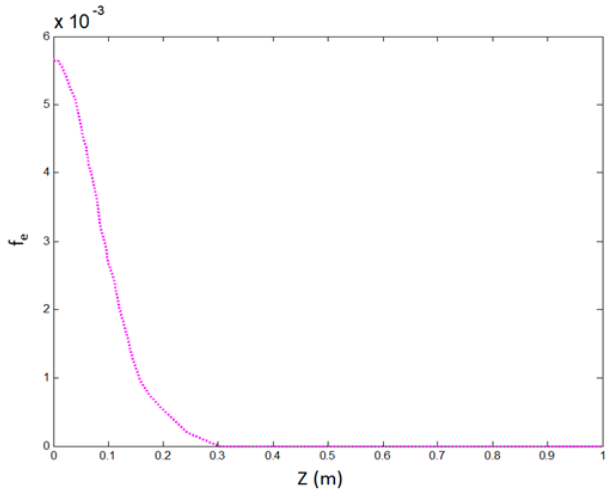


Figure 2. Fraction of resistance to external mass transfer (f_e) *vs.* reactor length (Z(m)).

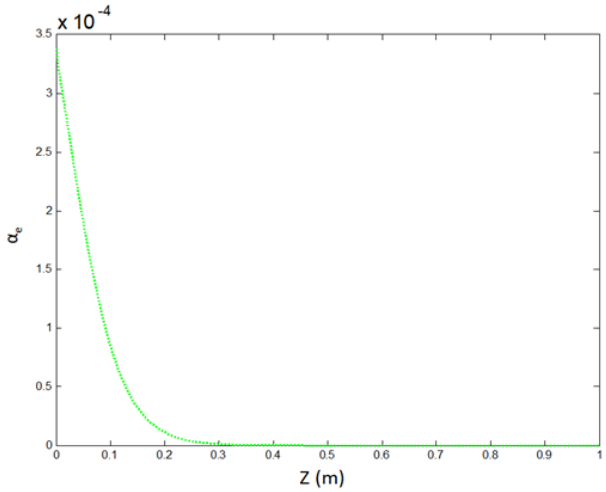


Figure 3. Fraction of resistance to external heat transfer (α_e) *vs.* reactor length (Z(m)).

Copyright © 2022, ISSN 1978-2993

considering that the diameter is that of the equivalent sphere to the cylindrical particle used in the study [32]. Figure 4 presents the experimental conversions and those obtained by simulation for a temperature of 623 K, a ratio H_2O/CO = 1 and for different (GHSV) (the ratio of the feed volumetric flow rate at standard conditions to the total catalyst volume). Figure 4 shows the good agreement between the experimental results of reference [32] and those of the numerical simulation that we obtained, and this, despite the fact that the proposed model relatively overestimates X_{CO} (the average difference compared to the experiment is 11%). This overestimation can be explained by several reasons, such as: (a) The fact that the reactor of the laboratory studied does not behave like an ideal plug reactor, given the existence of dispersive phenomena not taken into account by the model developed; (b) The fact that the model does not take into account the possible reduction in catalytic activity due to the formation of carbon on the catalyst. The probability of this hypothesis is not negligible, especially since the H_2O/CO ratio imposed in the experimental study is low (H_2O/CO = 1) [32].

The second comparison was made with the numerical study carried out by Marin *et al.* [23] who studied the case of an isobaric isoperibolic pilot reactor. We took into account all the operating conditions and the characteristics of the catalyst and the reactor detailed in [23]. Figure 5 shows the profile of the carbon monoxide conversion along the reactor obtained by Marin *et al.* [23] and this we obtained in the present study. According to the same figure, the difference between the two curves is acceptable even if our model slightly underestimates X_{CO} compared to the numerical study of Marin *et al.* [23] (an average difference of −7%). The difference between the two results can be explained by the difference between the models used to predict the intraparticle concentration and temperature profiles in each of the two studies. In fact, unlike our study in which a rigorous heterogeneous mono-dimensional model was adopted, in the study of Marin *et al.* [23], the model used is heterogeneous non-rigorous mono-dimensinal based on an expression of the apparent reaction rate taking into account resistances to intraparticle mass and heat transfers [23]. To conclude, this comparative study shows that there is a good agreement between the results found in the literature and those obtained by using the proposed model in this study.

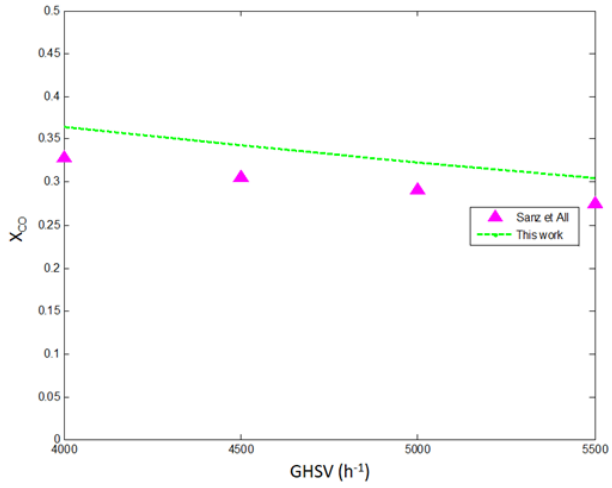


Figure 4. Comparison of simulation results of this study with experimental results of Sanz's *et al.* [32] study.

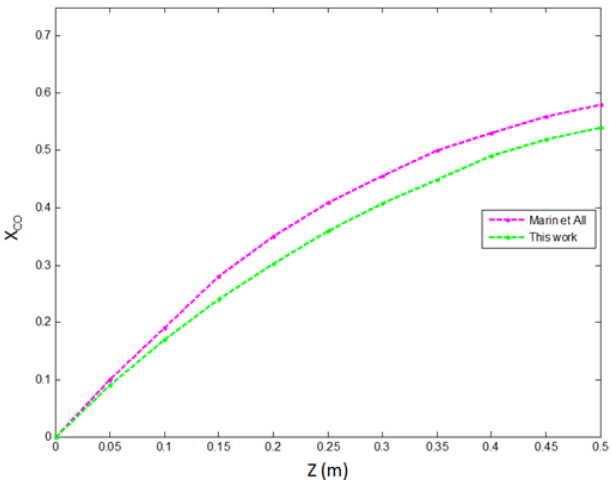


Figure 5. Comparison of simulation results of this study with simulation results of Marin's *et al.* [23] study.

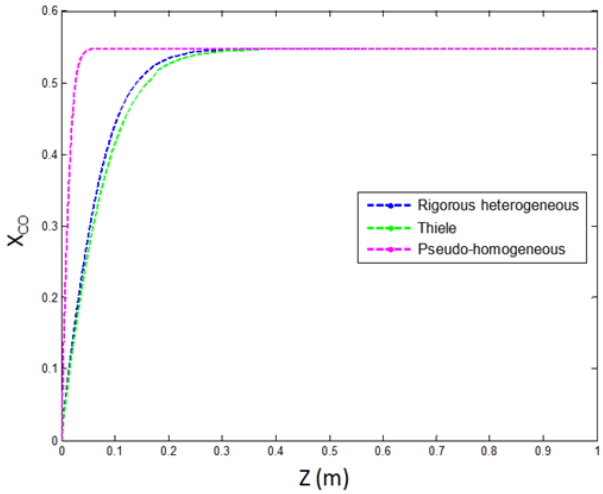


Figure 6. CO conversion (X_{CO}) *vs.* reactor length (Z(m)).

Copyright © 2022, ISSN 1978-2993

4.3 Determination of the Profiles of X_{CO}, T, and P Along the Reactor and Comparison between the Studied Models

Figures 6–8 show the profiles of X_{CO}, T, and P along the reactor using different models: pseudo-homogeneous, heterogeneous rigorous and heterogeneous adopting Thiele's approach. Figure 6 shows that whatever the model, the final conversion tends towards the same value imposed by the equilibrium (0.54), but the evolutions inside the reactor remain different. Indeed, due to intraparticle diffusional resistance, the conversion in heterogeneous models progresses slowly compared to the pseudo-homogeneous model. For the rigorous heterogeneous model, the equilibrium conversion rate corresponds to a longitudinal position close to Z = 0.245 m corresponding to a catalytic mass of 589.67 kg, while for the generalized Thiele's model, the longitudinal position corresponding to the equilibrium is close to Z = 0.265 m, the catalytic mass necessary to reach this equilibrium is 637.81 kg. In the absence of intraparticle diffusional resistance (pseudo-homogeneous model), chemical equilibrium is reached at a longitudinal position close to Z = 0.045 m, which corresponds to a catalytic mass of 108.3 kg. This clearly shows the detrimental effect of these diffusional resistances on the catalytic activity, and consequently, on the cost of the converter.

As this is an exothermic reaction taking place in an adiabatic reactor, the temperature along the installation increases until it reaches the equilibrium temperature (680 K), then it remains constant (Figure 7). For each model studied, this temperature is obtained at the longitudinal position corresponding to X_{CO} at the equilibrium. According to this figure, as for X_{CO}, the temperature increase is slow for the heterogeneous models compared to the pseudo-homogeneous model. This result is due to the fact that the heterogeneous models take into account the intraparticle diffusional resistance. In fact, these resistances slow down the reaction rate, which reduces the heat flow given off by the reaction, and consequently, this slows down the rise in temperature along the reactor.

It is also specified that this equilibrium temperature remains without adverse effect on the catalyst. In fact, the temperature should not exceed 823 K. If the temperature is very high, the catalyst will be rapidly deactivated by sintering of the particles [5].

Figure 8 shows linear pressure drops along the reactor which are almost the same for the three models ($dP/dZ \approx -10440$ Pa.m^{-1}). This leads to the conclusion that in the case studied, the slowing of the temperature rise caused by intraparticle diffusional resistances has no significant effect on the pressure drop along the reactor. The pressure drop at the outlet of the reactor is ≈8.67% of the inlet pressure. This value remains relatively high and exceeds the maximum admissible pressure drop in this type of reactor operating at such a pressure level (ΔP_{max} = 5%) [16]. It must be said that one of the major disadvantages of pressure drops is the increase in the speed of passage of the reaction flow through the catalyst bed, because this leads to a decrease in the contact time, and therefore, in the catalytic activity [5]. In addition, as has already been mentioned, the kinetics of the WGS is favorable to the pressure; therefore, a drop in the pressure decelerates it. In this studied case, mainly because of this

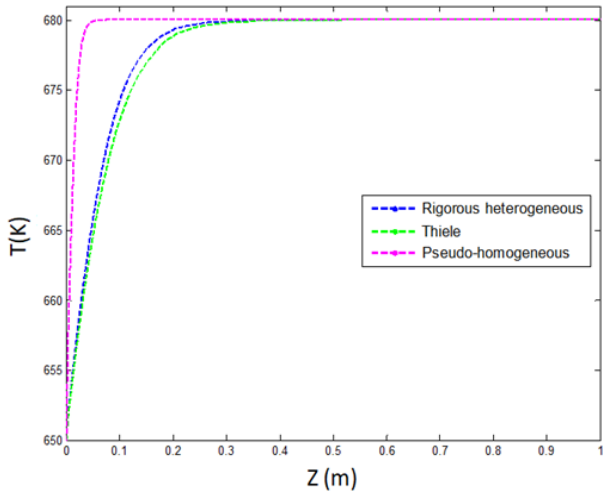


Figure 7. Temperature (T(K)) *vs.* reactor length (Z(m)).

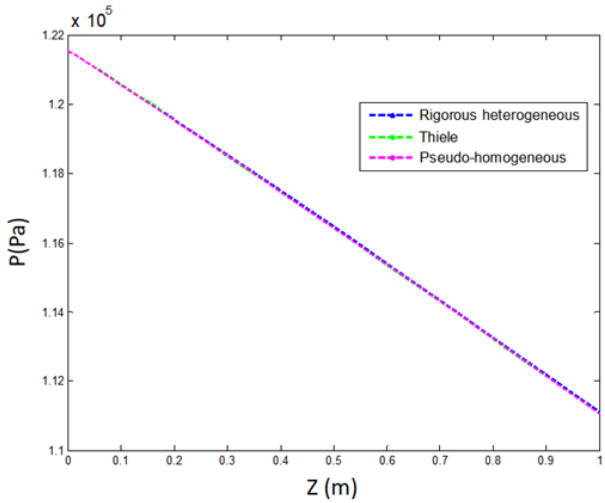


Figure 8. Pressure (P(Pa)) *vs.* reactor length (Z(m)).

Copyright © 2022, ISSN 1978-2993

pressure drop, the flow rate increases by 14.46% and the pressure scale-up factor, F_{pres}, drops by 4.35% between the inlet and the outlet of the reactor. Despite this, simulating the converter without considering the Ergun's equation did not reveal any significant change in the profiles of T and X_{CO}.

Figures 6–8 also show that results corresponding to the two heterogeneous models are very close, which leads to the conclusion that the simple Thiele's approach makes it possible to correctly describe the behavior of the reactor. This result is expected, because Thiele's approach is based on the domination of the strong diffusional regime [30,37] and the studied case corresponds well to this regime (low values of η_e and domination of intraparticle diffusional resistances).

4.4 Evaluation of the Effects of Intraparticle Diffusional Resistance on Reaction Rate and on Intraparticle Concentration Profiles.

In this paragraph, the rigorous heterogeneous model was exploited to study the impacts of intraparticle diffusional limitations on reaction rate and on intraparticle concentration profiles. Figure 9 shows the apparent and intrinsic reaction rate profiles. We specify that the apparent reaction rate is that taking into account the intragranular diffusional resistances corresponding to $\bar{r}$ (Equation (22)). Meanwhile, the intrinsic reaction rate is that without diffusion effects calculated using the bulk phase concentrations and temperatures corresponding to $r_{CO,f}$ (Equation (15)).

We see a drop in these two rates along the reactor until reaching the equilibrium, where $-r_{CO}$ keeps a zero value for the rest of the reactor. Indeed, even if the temperature increases the reaction rate constant K, under the effect of the reduction of the chemical driving force caused by the decrease in the concentrations of the reagents, the increase in the concentrations of the products and of the decrease in the equilibrium constant caused by the rise in temperature, the reaction rate decreases. This figure also shows that at Z = 0.245 m, the apparent reaction rate becomes almost negligible, which confirms that the equilibrium is very close to this axial position. We also notice that because of intraparticle diffusional resistance, the difference between the two types of reaction rate is important. In fact, the apparent reaction rate is 4–6 times slower than the intrinsic reaction rate.

Giunta *et al.* [4] observed this simultaneous decrease in the reaction rate with the drop in the effectiveness factor along an adiabatic WGS reactor also. To explain this result, the intraparticle concentrations profiles of the different chemical species involved in the reaction and the reaction rate profiles within the catalyst particle for different reactor axial positions were determined.

The intraparticle concentration gradients of CO, CO_2, H_2, and H_2O at the inlet of the reactor are shown in Figure 10. These gradients clearly mean that intraparticle diffusional resistances are present. Unlike reactants, whose concentrations decrease with penetration into the pellet, for products, the more one goes towards the center of the pellet, the more their concentrations increase, this is due to the conversion of the reactants inside the catalyst. Figure 10 shows also that the active zone, place of these concentration gradients, and

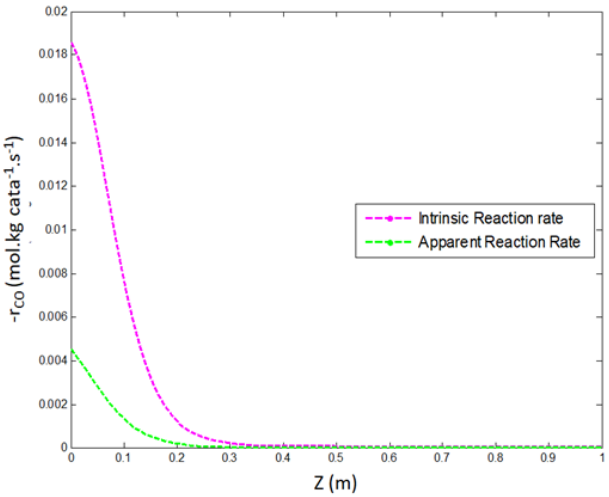


Figure 9. Reaction rate ($-r_{CO}$ (mol.kg.cat^{-1}.s^{-1})) *vs.* reactor length (Z(m)).

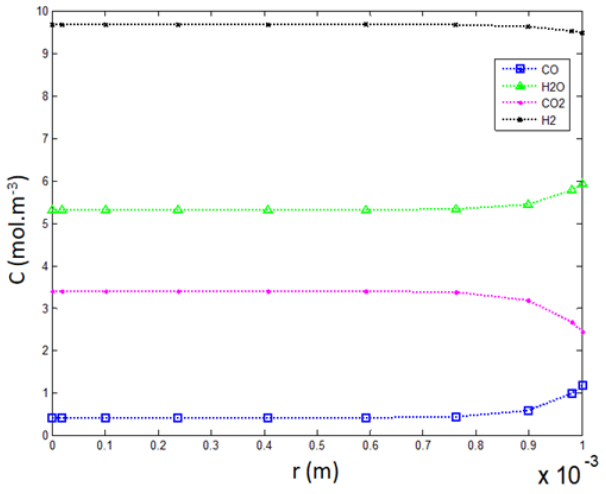


Figure 10. concentration profiles within the catalyst particle (Z = 0).

Copyright © 2022, ISSN 1978-2993

therefore concerned by the diffusion and by the chemical reaction, is located between the surface and 0.6 mm from the center of the pellet. Below this radial position, the concentration profiles are flat and thus signal the absence of diffusional activity and the cancellation of reaction rate. By advancing inside the reactor, under the effect of the rise in temperature, the decrease in the concentrations of the reactants, the increase in the concentrations of the products and the decrease in the reaction rate, the equilibrium (thermodynamics and chemical) within the pellet is reached at radial positions further and further from the center of the pellet. These results from the increasingly flattening intraparticle concentration profiles (Figures 10–12) and the production of the reaction closer and closer to the pellet surface. This means that less reactants can diffuse into the interior of the pore, resulting in reduced active area (Figures 10–12). This narrowing of the active area widens the difference between the intrinsic and the apparent reaction rate, thus leading to the decrease in the effectiveness factor (Figure 1). At Z = 0.245 m, the equilibrium is almost reached in the reactor, so the rate of the chemical reaction is cancelled out and intraparticle diffusion stops, which explains the flat concentration profiles shown in Figure 12.

As shown in Figure 13, there is a decrease in intraparticle reaction rate with penetration inside the particle which is due to resistance to intraparticle diffusion. Figure 13 shows also that because of the decrease in the reaction rate with progress through the reactor, reaction rates on the surface and within the pellet decrease. It is also seen that the narrowing of the active zones with advancement in the reactor results in the widening of the intraparticle space in which $-r_{CO} \approx 0$. In fact, at the reactor inlet, $-r_{COs}$ = 0.0185 mol.kg.cat^{-1}.s^{-1} and the active zone is located at [$r = 0.6\times10^{-3}$ m – $r = 10^{-3}$ m], at Z = 0.05 m, $-r_{COs}$ = 0.01416 mol.kg.cat^{-1}.s^{-1} and the active area is reduced to [$r = 0.7\times10^{-3}$ m – $r = 10^{-3}$ m] and finally to Z = 0.245 m, the reaction rate at the surface of the pellet drops to 4.3×10^{-4} mol.kg.cat^{-1}.s^{-1} and the active zone becomes very thin [$r = 0.9\times10^{-3}$ m – $r = 10^{-3}$ m].

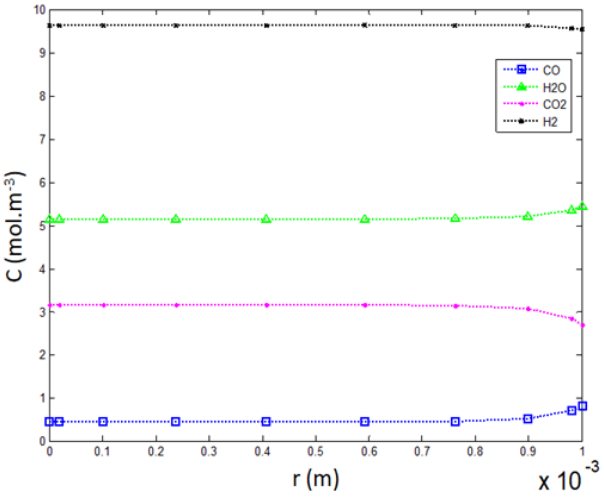


Figure 11. Concentration profiles within the catalyst particle (Z = 0.05 m).

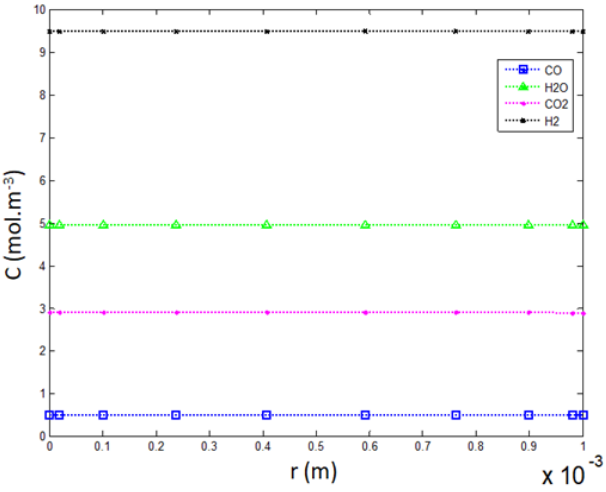


Figure 12. Concentration profiles within the catalyst particle (Z = 0.245 m).

4.5 Evaluation of the Effects of Pressure on the Reactor Behavior

Figure 14 shows the evolution of X_{CO} along the reactor for different inlet pressures. It is clear that with the rise in pressure, the axial position to reach the conversion at equilibrium (0.54) is reduced. therefore, the catalytic mass

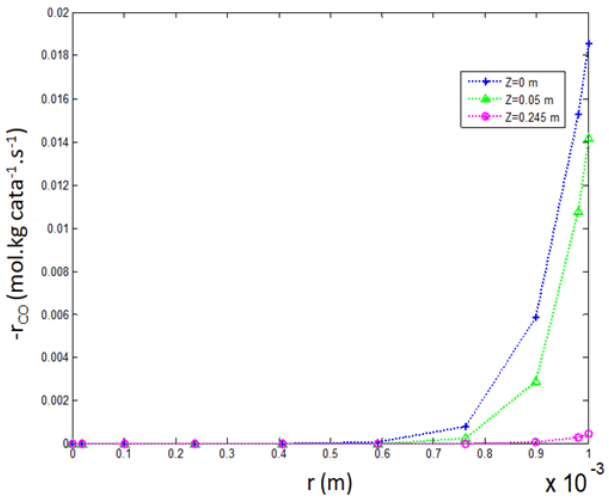


Figure 13. Reaction rate profiles within the catalyst particle for different reactor axial position.

Copyright © 2022, ISSN 1978-2993

necessary to reach this conversion decreases from 589.67 kg for the inlet pressure of 1.2 atm to 144.4 kg for the inlet pressure of 9.87 atm. This result is explained by the increase in the reaction rate at the inlet of the reactor and in the axial positions increasingly close to this inlet with the rise in pressure, because this rise in pressure allows both increase the Scale-up factor (F_{pres}) and the reactant concentrations (H_2O, CO). With this rise in the reaction rate towards the inlet of the installation, the consumption of the reactants and the achievement of equilibrium occurs increasingly close to the inlet of the converter.

Figure 15 shows the evolution of the effectiveness factor along the reactor for these different feed pressures. We notice that the increase in pressure reduces the effectiveness factor along the reactor, but this reduction in η_e does not inhibit the accelerating effect of the pressure on the reaction rate at the inlet of the converter and in the axial positions close to the reactor entrance. One can explain this drop in the efficiency factor by the fact that the rise in pressure accelerates the intrinsic reaction rate while it has no effect on the effective diffusivities.

The simulation results also showed that with the rise in pressure, the maximum temperature reached in the reactor does not increase significantly, and that the pressure drops become negligible (ΔP<1% for P_0 = 4.93 atm and P_0 = 9.87 atm). Finally, these simulations did not reveal significant external resistances to mass and heat transfer (f_{emax}<0.05 and α_{emax}<0.003).

4.6 Evaluation of the Effects of Feed Temperature and Reactants Feed Stream on the Reactor Behavior

Table 4 shows the effects of the feed temperature on the overall effectiveness factor of the catalyst at the inlet of the reactor and on dif-

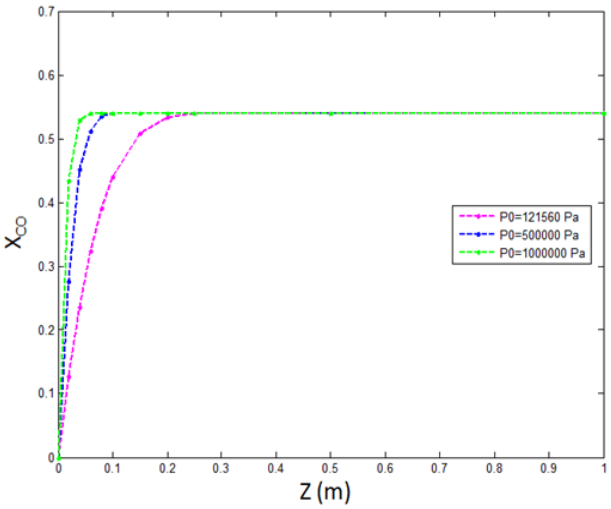


Figure 14. CO conversion (X_{CO}) *vs.* reactor length (Z(m)) for different inlet pressures.

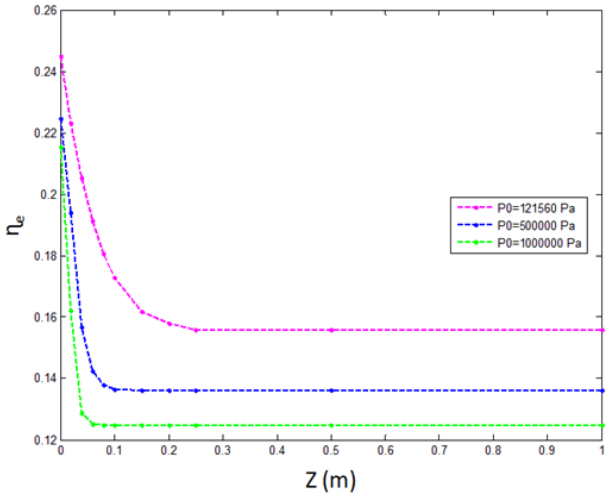


Figure 15. Overall effectiveness factor (η_e) *vs.* reactor length (Z(m)) for different inlet pressures.

Table 4. Effect of feed temperature on reactor behaviour.

T (Z = 0)	η_e (Z = 0)	T ($Z = L_t$)	X_{CO} ($Z = L_t$)	ΔP (%)
600	0.386	640	0.674	8.15
620	0.32	656.5	0.6233	8.44
635	0.2795	669	0.583	8.7
650	0.2451	680	0.54	8.8
664	0.2178	693	0.502	9.2

Table 5. Effect of feed stream of reactants on reactor behaviour.

$F_{reactant}$ (mol.s^{-1})	η_e (Z = 0)	T ($Z = L_t$)	X_{CO} ($Z = L_t$)	ΔP (%)
7.26	0.2002	652.4	0.07	6.6
10.8731	0.2276	668.7	0.39	7.8
14.514	0.2451	680	0.54	8.67
18.2205	0.2569	691.3	0.627	10.4
21.78	0.2659	700	0.682	12

Copyright © 2022, ISSN 1978-2993

ferent parameters at outlet (conversion of CO, temperature, percentage of pressure drop reported to the inlet pressure. Table 5 shows the effect of the reactants feed stream on the same parameters. It should be noticed that in all the simulations presented in this section, equilibrium is reached before reaching the outlet of the rector, *i.e.* the X_{CO} ($Z = L_t$) and T ($Z = L_t$) presented in these two tables correspond to X_{CO} and T in the equilibrium.

According to Table 4, the higher the feed temperature is, the lower the effectiveness factor at the inlet of the reactor is. This result is due to the fact that the rise in temperature causes an increase in the reaction rate constant K, while the effect of temperature on the effective diffusivities is not significant. This result is consistent with the results of several studies found in the literature on the effect of temperature on effectiveness factor [40,41]. According to Table 4, the rise in temperature causes a decrease in the conversion at the outlet of the reactor, because, according to Le Chatelier's principle [30], to oppose the increase in temperature, the equilibrium is shifted in the direction of the reverse reaction, which leads to the conversion drop. It is also noticed that the temperatures at the outlet of the reactor, mentioned in the table, remain bearable by the catalyst and that the rise in temperature does not have a great influence on the pressure drop in the reactor.

According to Table 5, it can be observed that the effectiveness factor increases with the increase of the reactants feed streams. In fact, this rise in reactants flow rates is accompanied by a rise of the reactants concentration. Under these conditions, the consumption of the reactants requires larger active zones to reach equilibrium within the pellet, which leads to the increase in η_e. The rise in reactants concentrations increases the reaction rate at the inlet of the reactor. Because of this increase, the conversion and the temperature required for the cancellation out of the reaction rate, and therefore, for the achievement of the equilibrium, rise as shown in Table 5. It can also be seen that these temperatures remain bearable by the catalyst. Finally, as in agreement with Ergun's equation, the increase in the feed volume flow rate, and hence the increase in the superficial velocity, leads to an increase in the pressure drop in the reactor.

The simulation results presented in this paragraph did not reveal significant interfacial resistances to mass and heat transfer, as f_e does not exceed 6.6×10^{-3} and α_e does not exceed 5×10^{-4}. Other parameters can also affect the process performance such as the thermal regime in the reactor, the size and shape of the catalytic particle and the composition of the catalyst.

5. Conclusion

This work constitutes a numerical study focusing on the modelling and simulation of a WGS adiabatic catalytic reactor operating at low pressures (1.2–1.097 atm). Through this study, we were able to evaluate the behaviour of this converter when the pressure level is close to atmospheric pressure. The rigorous model developed for this study has been validated with experimental and simulation results published in the literature. Under the conditions of low pressures studied, the resistances to interfacial mass and heat transfer are very low and the rise in temperature in the reactor is bearable by the catalyst. On the other hand, the pressure losses exceed the tolerable limit and the intraparticle diffusion resistances are important. In this case of strong diffusional regime domination, the effectiveness factor of the catalyst is low, and therefore, the catalytic mass necessary to achieve the desired carbon monoxide conversion is high. This study showed that even if the increase in pressure causes a decrease in the effectiveness factor, the higher the pressure, the more the catalytic mass necessary to achieve the conversion at equilibrium is reduced. This study also revealed that it is possible to reduce the intraparticle diffusional limitations and to improve the process yield by acting on the feed temperature and on the reactants feed stream. For a good improvement of reactors operating at low pressures, the egg-shell catalyst can be explored. In fact, thanks to this catalyst, it is possible to have a large particle size which reduce the pressure drops. At the same time, given that it has been shown that the diffusional resistances are strong, that a large part of the volume of the catalytic particle is inactive and that the active intraparticle zone concerned by the diffusion and by the chemical reaction is located close to the surface, the use of the egg-shell technique, allows to reduce catalyst usage, and the intraparticle diffusional resistances thanks to the thin active catalytic layer coating the inert spherical support characterising this type of catalyst. As a perspective for this study, it seems very useful to model and simulate a WGS converter operating at low pressures in the presence of this type of catalyst.

Copyright © 2022, ISSN 1978-2993

Acknowledgement

The authors would like to acknowledge the Moroccan Ministry of Higher Education, Scientific Research and Innovation.

References

[1] Chen, W.H., Lin, M.R., Jiang, T.L., Chen, M.H. (2008). Modeling and simulation of hydrogen generation from high temperature and low-temperature water gas shift reactions. *International Journal of Hydrogen Energy,* 33, 6644–6656. DOI: 10.1016/j.ijhydene.2008.08.039.

[2] Callaghan, C.A. (2006). Kinetics and Catalysis of the Water-Gas-Shift Reaction: A Microkinetic and Graph Theoretic Approach. *Ph.D. Dissertation,* Department of Chemical Engineering, Worcester Polytechnic Institute.

[3] Smith, R.J., Loganathan, M., Shantha,M. S.(2010). A Review of the Water Gas Shift Reaction Kinetics. *International Journal of Chemical Reactor Engineering,* 8, 1–32. DOI: 10.2202/1542-6580.2238.

[4] Giunta, P., Amadeo, N., Laborde, M. (2006). Simulation of a low temperature water gas shift reactor using the heterogeneous model/application to a pem fuel cell. *Journal of Power Sources,* 156, 489–496. DOI: 10.1016/j.jpowsour.2005.04.036.

[5] Lang, C. (2016). Développement de catalyseurs pour la réaction de conversion du gaz à l'eau dans le cadre de la production d'hydrogène par vapogazéification de la biomasse. *Ph.D. Dissertation,* Institut de Chimie et Procédés pour l'énergie, l'environnement et la santé, Strasbourg University.

[6] Lee, S.B., Cho, W., Park, D.K., Yoon, E.S. (2006). Simulation of fixed bed reactor for dimethyl ether synthesis. *Korean Journal of Chemical Engineering*, 23, 522–530. DOI: 10.1007/BF02706789.

[7] Raje ,A., Inga, J. R., Davis, B.H. (1997). Fischer-Tropsch synthesis: process considerations based on performance of iron-based catalysts. *Fuel*, 76, 273–280. DOI: 10.1016/S0016-2361(96)00185-8.

[8] Skrzypek, J., Lachowska, M., Grzesik, M., Słoczyński, J., Novak, P. (1995). Thermodynamics and kinetics of low-pressure methanol synthesis. *The Chemical Engineering Journal*, 58, 101–108. DOI: 10.1016/0923-0467(94)02955-5.

[9] Schumacher, N., Boisen, A., Dahl,S., Gokhale,A., Kandoi,S., Grabow, L., Dumesic, J., Mavrikakis, M., Chorkendorff, I. (2005). Trends in Low-Temperature Water-Gas Shift Reactivity on Transition Metals. *Journal of Catalysis*, 229, 265–275. DOI: 10.1016/j.jcat.2004.10.025.

[10] Bohlbro, H. (1964). The kinetics of the Water-Gas Conversion IV. Influence of Alkali on the Rate Equation. *Journal of Catalysis*, 3, 207–215. DOI : 10.1016/0021-9517(64)90168-X.

[11] Keiski, R.L., Salmi, T., Pohjola, V.J. (1992). Development and verification of a simulation model for a non-isothermal water gas-shift reactor. *The Chemical Engineering Journal,* 48, 17–29. DOI: 10.1016/0300-9467(92)85003-R.

[12] Keiski, R.L., Desponds, O., Chang, Y.F., Somorjai, G.A. (1993). Kinetics of the water-gas shift reaction over sevral alkane activation and water-gas shift catalyst. *Applied Catalysis A: General*, 101, 317–338. DOI: 10.1016/0926-860X(93)80277-W.

[13] Koryabkina, N.A., Phatak, A.A., Ruettinger, W.F., Farrauto, R.J., Ribeiro, F.H. (2003). Determination of kinetic parameters for the water-gas-shift reaction on copper catalysts under realistic conditions for fuel cell applications. *Journal of Catalysis*, 217, 233–239. DOI: 10.1016/S0021-9517(03)00050-2.

[14] Hla, S.S., Park, D., Duffy, G.J., Edwards, J.H., Roberts, D.G. (2009). Kinetics of high-temperature water-gas shift reaction over two iron-based commercial catalysts using simulated coal-derived syngases. *Chemical Engineering Journal,* 146, 148–154. DOI :10.1016/j.cej.2008.09.023.

[15] Adams, T.A., Barton, P.I. (2009). A dynamic two-dimensional heterogeneous model for water gas shift reactors. *International Journal of Hydrogen Energy,* 34, 8877–8891. DOI: 10.1016/j.ijhydene.2009.08.045.

[16] Maklavany, D.M., Shariati, A., Nikou, M.R.K., Roozbehani, B. (2017). Hydrogen Production via Low Temperature Water Gas Shift Reaction: Kinetic Study, Mathematical Modeling, Simulation and Optimization of Catalytic Fixed Bed Reactor using gPROMS. *Chemical Product and Process Modeling*. 12, 20160063. DOI: 10.1515/cppm-2016-0063.

[17] Hwang, S., Smith, R. (2004). Heterogeneous catalytic reactor design with optimum temperature profile I: application of catalyst dilution and side-stream distribution. *Chemical Engineering Science*, 59, 4229–4243. DOI: 10.1016/j.ces.2004.05.037.

Copyright © 2022, ISSN 1978-2993

[18] Elnashaie, S.S.E.H., Alhabdan, F.M. (1989). Mathematical modelling and computer simulation of industrial Water-Gas Shift Converters. *Mathematical and Computer Modelling*, 12, 1017–1034. DOI: 10.1016/0895-7177(89)90208-2.

[19] van Dijk, H.A.J., Cohen, D., Hakeem, A.A., Makkee, M., Damen, K. (2014). Validation of a water–gas shift reactor model based on a commercial FeCr catalyst for pre-combustion CO_2 capture in an IGCC power plant. *International Journal of Greenhouse Gas Control*, 29, 82–91. DOI: 10.1016/j.ijggc.2014.07.005.

[20] Rosner, F., Rao, A., Samuelsen, S. (2020). Water gas shift reactor modelling and new dimensionless number for thermal management/design of isothermal reactors. *Applied Thermal Engineering,* 173, 1–19. DOI: 10.1016/j.applthermaleng.2020.115033.

[21] Francesconi, J.A., Mussati, M.C., Aguirre, P.A. (2007). Analysis of design variables for water-gas-shift reactors by model-based optimization. *Journal of Power Sources,* 173, 467–477. DOI: 10.1016/j.jpowsour.2007.04.048.

[22] Davis, M.E., Davis, R.J. (2003). *Fundamentals of Chemical Reaction Engineering*. Edition. New York: McGraw-Hill Companies.

[23] Marin, P., Diez, F.V., Ordonez, S. (2012). Fixed bed membrane reactors for WGSR-based hydrogen production: Optimisation of modelling approaches and reactor performance. *International Journal of Hydrogen Energy*, 37, 4997–5010. DOI: 10.1016/j.ijhydene.2011.12.027.

[24] Saw, S.Z., Nandong, J. (2016). Simulation and control of water-gas shift packed bed reactor with inter-stage cooling. *IOP Conf. Series: Materials science and Engineering,* 121, 1–10. DOI: 10.1088/1757-899X/121/1/012022.

[25] Soit, A.C., Dumbrava, I., Sandu, V.C., Cormos, A.M. (2019). Modelling and Simulation of Water Gaz Shift Reactor Using Comsol Multiphysics. *Studia UBB Chemia*, LXIV, 4, 19–29. DOI: 10.24193/subbchem.2019.4.02.

[26] Levent, M. (2001). Water–gas shift reaction over porous catalyst: temperature and reactant concentration distribution. *International Journal of Hydrogen Energy,* 26, 551–558. DOI: 10.1016/S0360-3199(00)00116-6.

[27] Hallac, B.B. (2014). Kinetic Experimental and Modeling Studies on Iron-Based Catalysts Promoted with Lanthana for the High-Temperature Water-Gas Shift Reaction Characterized with Operando UV-Visible Spectroscopy and for the Fischer-Tropsch Synthesis. *Ph.D. Dissertation,* Department of Chemical Engineering, Brigham Young University.

[28] El Bazi, W., El-Abidi, A., Kadiri, M.S., Yadir, S. (2018). Modeling and Simulation of a Water Gas Shift Reactor operating at a low pressure. *International Journal of Innovation Engineering and Science Research*, 2, 47–57.

[29] Atwood, K., Arnold, M.R., Appel, E.G. (1950). Water-Gas Shift Reaction. Effect of Pressure on Rate over an Iron- Oxide-Chromium Oxide Catalyst. *Industrial & Engineering Chemistry,* 42, 1600–1602. DOI: 10.1021/ie50488a038.

[30] Villermaux, J. (1993). *Génie de la réaction chimique*. Edition. Paris: Tec & Doc Lavoisier.

[31] Ducamp, J., Bengaouer, A., Baurens, P., Fechete, I., Turek, P.T., Garin, F. (2018). Statu quo sur la methanation du dioxyde de carbone: une revue de la littérature. *Comptes Rendus Chimie*, 21(3–4), 427–469. DOI: 10.1016/j.crci.2017.07.005.

[32] Sanz, R., Calles, J.A., Alique, D., Furones, L., Ordonez, S., Marin, P. (2015). Hydrogen production in a Pore-Plated Pd-membrane reactor: Experimental analysis and model validation for the Water Gas Shift reaction. *International Journal of Hydrogen Energy*, 40, 3472–3484. DOI: 10.1016/j.ijhydene.2014.11.120.

[33] Santacesaria, E., Tesser, R. (2018). *The Chemical Reactor from Laboratory to Industrial Plant : A Modern Approach to Chemical Reaction Engineering with Different Case Histories and Exercises*. Edition. Cham: Springer.

[34] Wakao, N., Kaguei. S., Funazkri, T. (1979). Effect of fluid dispersion coefficients on particle-to-fluid heat transfer coefficients in packed-beds – Correlation of Nusselt numbers. *Chemical Engineering Science,* 34, 325–336. DOI: 10.1016/0009-2509(79)85064-2.

[35] Villadsen, J.V., Stewart, W.E. (1967). Solution of boundary-value problems by orthogonal collocation. *Chemical Engineering Science,* 22, 1483–1501. DOI: 10.1016/0009-2509(67)80074-5.

[36] Dumez, F.J., Forment, G.F. (1976). Dehydrogenation of 1-Butene into Butadiene. Kinetics, Catalyst Coking, and Reactor Design. *Industrial & Engineering Chemistry Process Design and Development,* 15, 291–301. DOI: 10.1021/i260058a014.

[37] Forment, G.F., Bischoff, K.B., Wilde, J.D. (2010). *Chemical Reactor Analysis and Design*. Edition. Hoboken: John Wiley & Sons, Inc.

Copyright © 2022, ISSN 1978-2993

[38] Missen, R.W., Mims, C.A., Saville, B.A. (1999). *Introduction to Chemical Reaction Engineering And Kinetics*. Edition. Danvers: John Wiley & Sons.

[39] Mendes, D., Chibante, V., Mendes, A. Madeira, L.M. (2010). Determination of the Low-Temperature Water-Gas Shift Reaction Kinetics Using a Cu-Based Catalyst. *Industrial & Engineering Chemistry Research,* 49, 11269–11279. DOI: 10.1021/ie101137b.

[40] Zhang, L., Zhang, H.T., Ying, W.Y., Fang, D.Y. (2014). The Simulation of an Industrial Fixed Bed Reactor for Methanol Dehydration to Dimethyl Ether. *Energy Sources, Part A: Recovery, Utilization, and Environmental Effects*, 36, 2166–2174. DOI: 10.1080/15567036.2012.750404.

[41] Chabot, G., Guilet, R., Cognet, P., Gourdon, P. (2015). A mathematical modeling of catalytic milli-fixed bed reactor for Fischer–Tropsch synthesis: Influence of tube diameter on Fischer-Tropsch selectivity and thermal behavior. *Chemical Engineering Science*, 127, 72–83. DOI: 10.1016/j.ces.2015.01.015.

Copyright © 2022, ISSN 1978-2993